Supplement of The Cryosphere, 17, 1497–1512, 2023
https://doi.org/10.5194/tc-17-1497-2023-supplement

The Cryosphere
Open Access

Supplement of

High mid-Holocene accumulation rates over West Antarctica inferred from a pervasive ice-penetrating radar reflector

Julien A. Bodart et al.

Correspondence to: Julien A. Bodart (julien.bodart@ed.ac.uk)

Supplementary Information

Assessing the suitability of the local-layer approximation

To quantify to what extent the assumptions used in the 1-D model are valid for estimating Holocene accumulation rates between the 4.72 ka IRH and the present, we calculated horizontal gradients in modern ice thickness and accumulation rates over the WAIS, and combined these to calculate the non-dimensional parameter D spanning the catchments where the 4.72 ka IRH was traced (Waddington et al., 2007) (Fig. S1).

The input datasets used for this calculation were modern ice thickness from BedMachine v2 (Morlighem, 2020), modern surface mass balance (1979 – 2019) from RACMO 2.3p2 (Van Wessem et al., 2018), and modern surface velocities (1996 – 2016) from the InSAR MEaSUREs v2 dataset (Rignot et al., 2017). These were all regridded to a single 1-km grid using bilinear interpolation and smoothed using an exponentially decaying filter equivalent to ten ice thicknesses in length, before subsampling the data to a common 5-km grid for data analysis. Following MacGregor et al. (2016), we re-calculated surface speed directions for slower ice-flow regions (<100 m a^{-1}) in the interior of the ice sheet using surface-elevation gradients from the BedMachine product. To calculate L_{path} (Fig. S1a), we then produced a reverse flowline for each grid cell based on modern ice-surface velocity, $\bar{u}$, and calculated where, along the reverse flowline, we obtained age, a:

$$L_{path} = \bar{u}\, a \,. \tag{S1}$$

We then interpolated the ice-thickness and accumulation-rate grids onto each flowline and conducted a first-order polynomial fit to obtain the ice-thickness and accumulation-rate gradients along the flowline. The ensuing gradients were then combined with the mean values along the flowline ($\bar{H}$ and $\bar{b}$) to calculate the characteristic lengths L_H and $L_{\dot{b}}$ (Fig. S1b-c), as follows:

$$\frac{1}{L_H} = \left|\frac{1}{\bar{H}}\frac{dH}{dx}\right|, \tag{S2}$$

$$\frac{1}{L_{\dot{b}}} = \left|\frac{1}{\bar{b}}\frac{d\dot{b}}{dx}\right|. \tag{S3}$$

Taken together, the ice-thickness and accumulation-rate gradients were combined to obtain a characteristic length scale, which was used to compare with L_{path} to generate the non-dimensional parameter D (Fig. S1d):

$$D = L_{path}\left(\frac{1}{L_H} + \frac{1}{L_{\dot{b}}}\right). \tag{S4}$$

Values where $D \ll 1$ indicate that local horizontal gradients in ice thickness and accumulation rates have a smaller effect on IRH depth of age a, and hence we assume that the LLA is valid for estimating accumulation rates for an IRH of age a (Waddington et al., 2007; MacGregor et al., 2009) (Sect. 2.2.1).

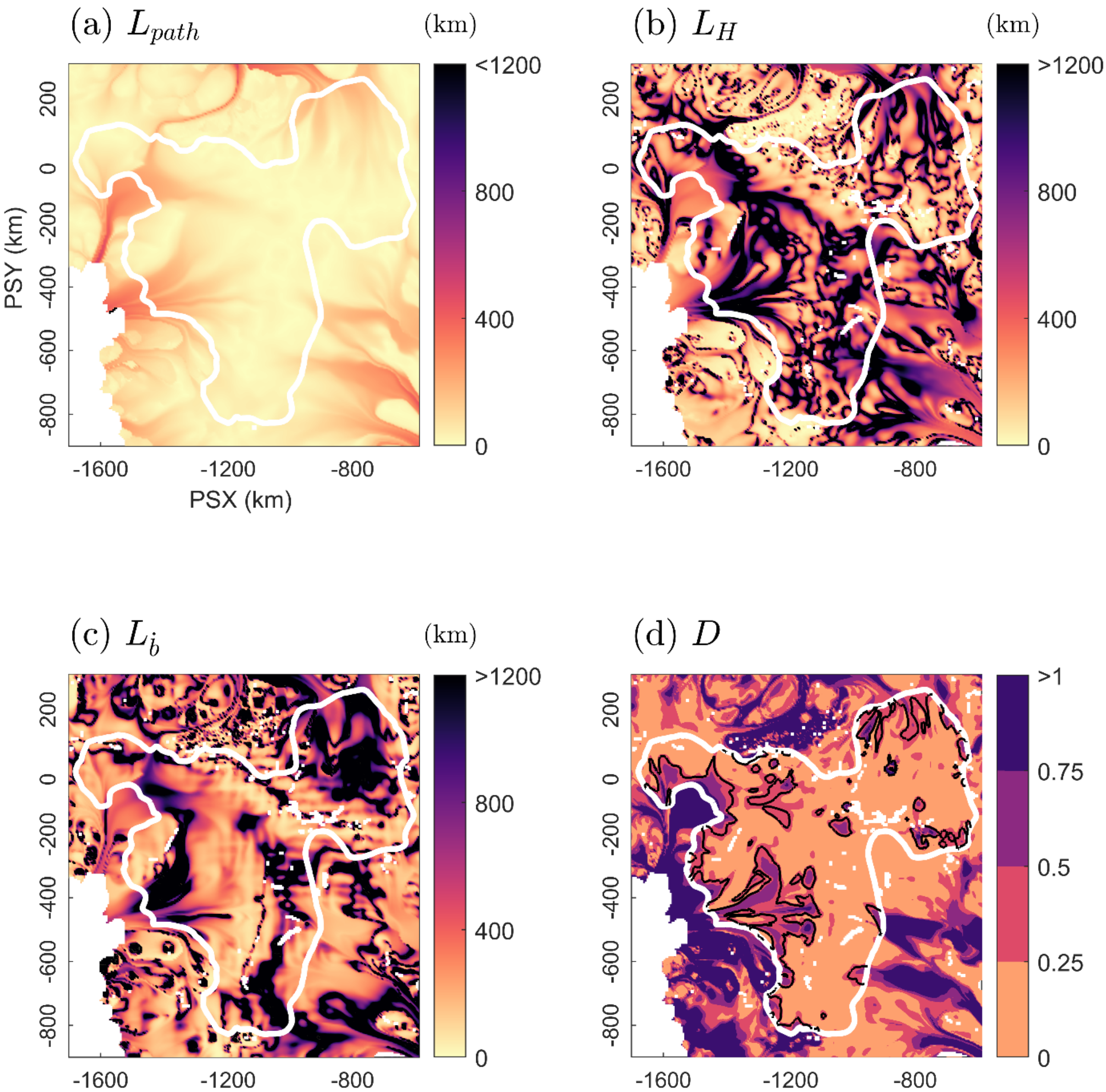

Figure S1. Suitability of the Local-Layer Approximation over the Pine Island, Thwaites, and Institute and Möller ice-stream catchments for the 4.72 ka IRH. (a) Horizontal path length, L_{path}, of a 4.72 ka particle of ice to reach its present location, calculated using modern surface velocities (Rignot et al., 2017). (b) Characteristic length of ice-thickness variability, L_H, along the 4.72 ka particle path, estimated using modern ice thickness measurements from BedMachine v2 (Morlighem, 2020). (c) Characteristic length of accumulation variability, $L_{\dot{b}}$, along the 4.72 ka particle path, estimated using modern modelled surface mass balance data from RACMO2 (Van Wessem et al., 2018). (d) The D parameter for the 4.72 ka IRH used to quantify the suitability of the LLA for the survey area (black contours represent the upper limit of the interquartile range for the D parameter ($D \leq 0.34$), whereby all values situated inside of this boundary may satisfy the D $\ll$ 1 criteria and those outside may require re-evaluating with the use of multi-dimensional models; see blue contours in Figure 4 of the main manuscript). The white outline represents the model domain boundary used to model Holocene accumulation rates where $D \leq 1$, whereas the black outline represents the upper limit of the interquartile range for the D parameter (i.e. $D \leq 0.34$) which we use to assess the level of confidence in the inferred Holocene accumulation rates.

Estimating uncertainty in inferred accumulation rates

Because the Nye model does not directly take into account the effect of strain rates on IRH depth and position within the ice column, it is not possible to assess its impact on the inferred accumulation rates, particularly in areas where strain rates are higher and the IRHs are deeper in the ice (e.g. the downstream section of our grid where ice flow is faster; Figs. 1-2 of the main paper). In turn, this limits our ability to quantify the model's structural uncertainty. Because the model's structural uncertainty is likely larger than that related to the IRH age (Section 2.2 of the main paper), it is important to quantify it to assess the significance of accumulation-rate change from modern values that we detect.

To overcome this issue, we used the shallow-strain rate model developed by MacGregor et al. (2016) which directly includes a strain-rate parameter that is independent from ice thickness, rather than one that is tied to ice thickness, as in the Nye model. The accumulation rates produced by this model are then used here to estimate lower and upper bounds in the accumulation rates that partly consider the effect of non-Nye vertical strain on the ice column and thus on the accumulation rate needed to reproduce the depth of the 4.72 ka IRH in the Nye model. The shallow-strain rate model for age, a, is:

$$a(z) = \frac{1}{\dot{\varepsilon}_{zz}^{a}} \ln\left(\frac{\dot{b}_a + \dot{\varepsilon}_{zz}^{a} z_a}{\dot{b}_a}\right). \qquad \text{(Eq. S5)}$$

The strain-rate parameter in Eq. (S5) would typically be $\dot{\varepsilon}_{zz}^{a}$ from Figure S2a, but because this is calculated based on the results from Eq. (1) it is not independent from the inferred accumulation rates presented here and is thus not a suitable input for evaluating accumulation-rate uncertainty inferred from the Nye model. In the absence of well-constrained vertical strain rates across our grid, by continuity, we used the longitudinal strain rates ($\dot{\varepsilon}_{xx}$; Fig. S2b) as an alternative to $\dot{\varepsilon}_{zz}^{a}$ in the shallow-strain rate model (ignoring lateral strain).

These were calculated from gradients in the x and y-direction for modern surface speeds ($\bar{u}$) projected onto the appropriate surface velocity unit vectors ($\hat{u}_{||}$) (MacGregor et al., 2013):

$$\dot{\varepsilon}_{xx} = \frac{\partial u}{\partial x} = \overline{\nabla}|\bar{u}| \cdot \hat{u}_{||}. \qquad \text{(Eq. S6)}$$

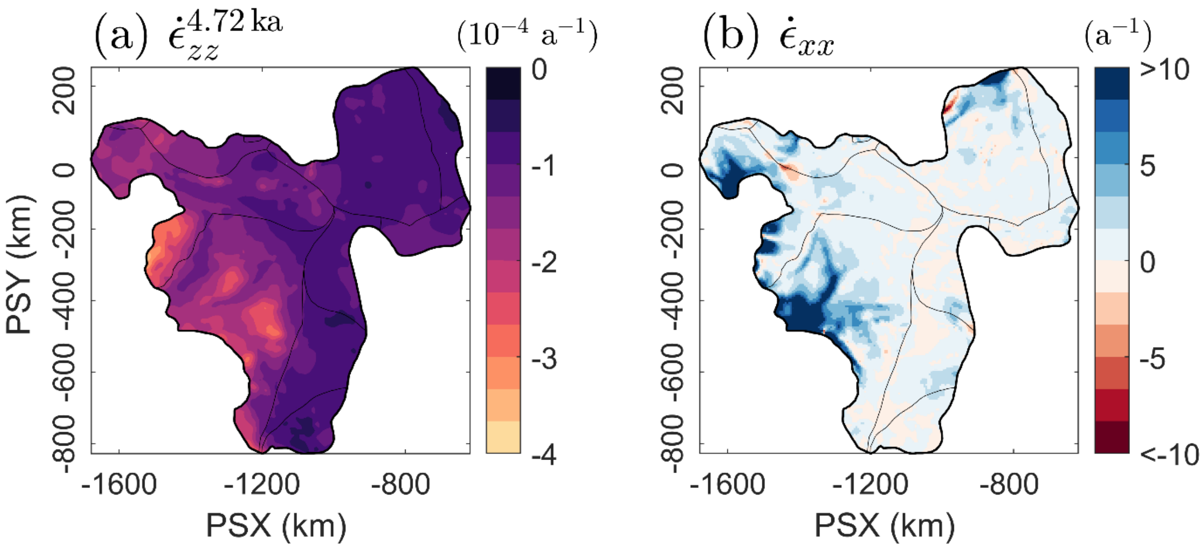

Figure S2. Strain rate patterns across the survey area. (a) Mean Nye-inferred vertical strain rates, $\dot{\varepsilon}_{zz}^{a}$, for the 0-4.72 ka portion of the ice column calculated from Eq. (2). (b) Longitudinal strain rates, $\dot{\varepsilon}_{xx}$, obtained from Eq. (S6).

To assess whether $\dot{\varepsilon}_{xx}$ can be used as a proxy for $\dot{\varepsilon}_{zz}^{a}$, we solved Eq. S5 for $\dot{b}_a$, replaced $\dot{\varepsilon}_{zz}^{a}$ for $\dot{\varepsilon}_{xx}$, and then compared the accumulation-rate results inferred from the shallow-strain model to the Nye-inferred accumulation rates over our grid from Figure 3a. Note that $\dot{\varepsilon}_{xx}$ can only be used as a proxy for $\dot{\varepsilon}_{zz}^{a}$ where $\dot{\varepsilon}_{xx} > 0$, as positive $\dot{\varepsilon}_{zz}^{a}$ values are typically only found in areas where the ice column is expanding, such as the ablation zone, and are thus non-physical for our model domain. As a result, all negative $\dot{\varepsilon}_{xx}$ values were replaced by extremely low, but positive strain-rate values (10^{-7} a^{-1}). The results shown in Figure S3 demonstrate that both the Nye and shallow-strain models produce similar results, but with decreasing similarity where $D > 0.34$, which is likely related to ice-dynamical processes affecting the assumptions of the Nye model further downstream (Fig. S4).

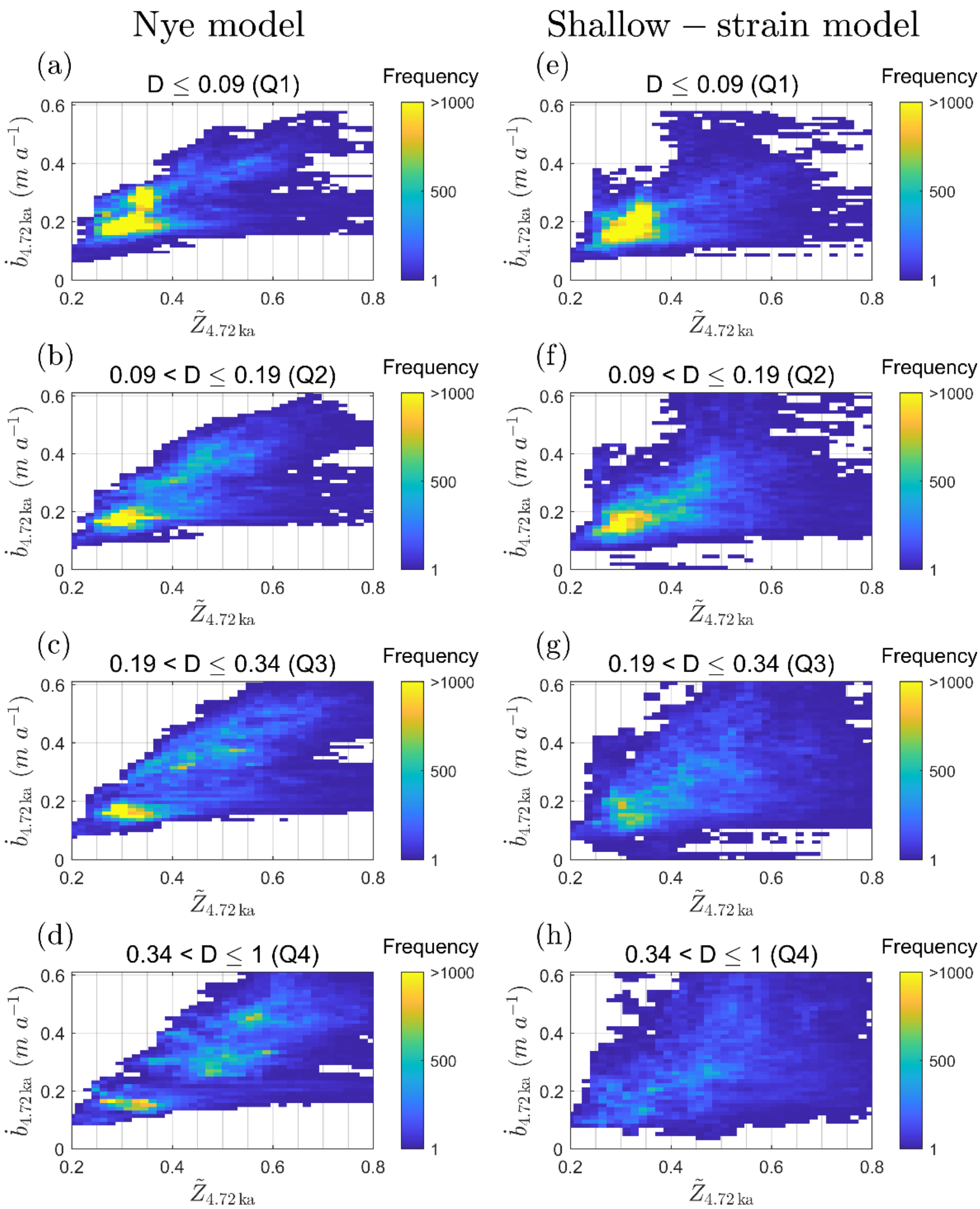

Figure S3. Histograms of inferred accumulation rates from the Nye (a-d) and the shallow-strain rate (e-h) models plotted against normalised IRH depths and binned into the four D quartiles (e.g. panels a and e are for all grid cells that fall within the lower quartile (Q1), b and f for all those that fall within the second quartile (Q2), etc; Sect. 2.2.1 of the main paper).

This analysis increases confidence that $\dot{\varepsilon}_{xx}$ can be used in the shallow-strain rate model from MacGregor et al. (2016) as a proxy for the vertical strain parameter, $\dot{\varepsilon}^{a}_{zz}$, to infer accumulation rates over the time period and location considered here, and thus ultimately has value for constraining uncertainty in the Nye-inferred accumulation rates (Fig. 3a). While this method likely produces more conservative uncertainty estimates than with the more challenging use of inverse flow-band models that solves for the effect of changing flow, temperature and strain conditions along targeted flow bands, it enables a straightforward uncertainty quantification across a large area.

We then produced two sets of upper and lower accumulation-rate uncertainties ($\dot{b}^{Low}_{4.72\ ka}$ and $\dot{b}^{High}_{4.72\ ka}$) for each of the following products over our grid: (1) using the Nye model from Eq. 1 with the IRH age uncertainty (± 0.28 ka); and (2) same as (1) but using the shallow strain-rate model from Eq. S5 using $\dot{\varepsilon}_{xx}$ as a proxy for $\dot{\varepsilon}^{a}_{zz}$. We then calculated the maximum $\dot{b}^{Low}_{4.72\ ka}$ and $\dot{b}^{High}_{4.72\ ka}$ values for each grid cell (Fig. S4a-b) and combined these to provide a relative uncertainty to the Nye-inferred accumulation rates (Fig. S4c). The largest relative uncertainties to the Nye-inferred accumulation rates (> 70%) are found primarily across the downstream end of Thwaites Glacier, and to a smaller extent over the edges of the grid of Pine Island Glacier and Institute and Möller Ice Streams where longitudinal strain rates are higher due to faster flowing ice. Relatively low uncertainties are found across the Amundsen-Weddell-Ross divide and most of the region where $D \leq 0.34$.

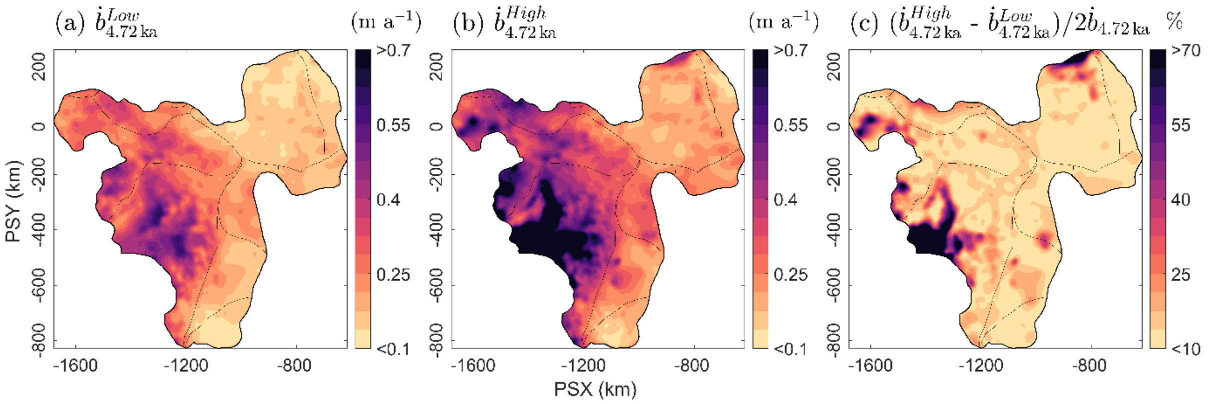

Figure S4. Uncertainties in inferred accumulation rates based on the radar and ice-core age uncertainties and from the accumulation rates returned from the shallow-strain rate model (Eq. S5). (a) Lower bound accumulation estimates, which are the product combination of the combined uncertainty from the radar and ice-core uncertainties in the age of the 4.72 ± 0.28 ka IRH (Muldoon et al., 2018; Bodart et al., 2021) and the accumulation rate returned from the shallow-strain rate model. (b) same as (a) but for the upper bounds in accumulation rates. (c) Relative uncertainty in Nye-inferred accumulation rates for the 4.72 ka IRH (Fig. 3a) based on the lower and upper bound estimates from Figures S4a-b.

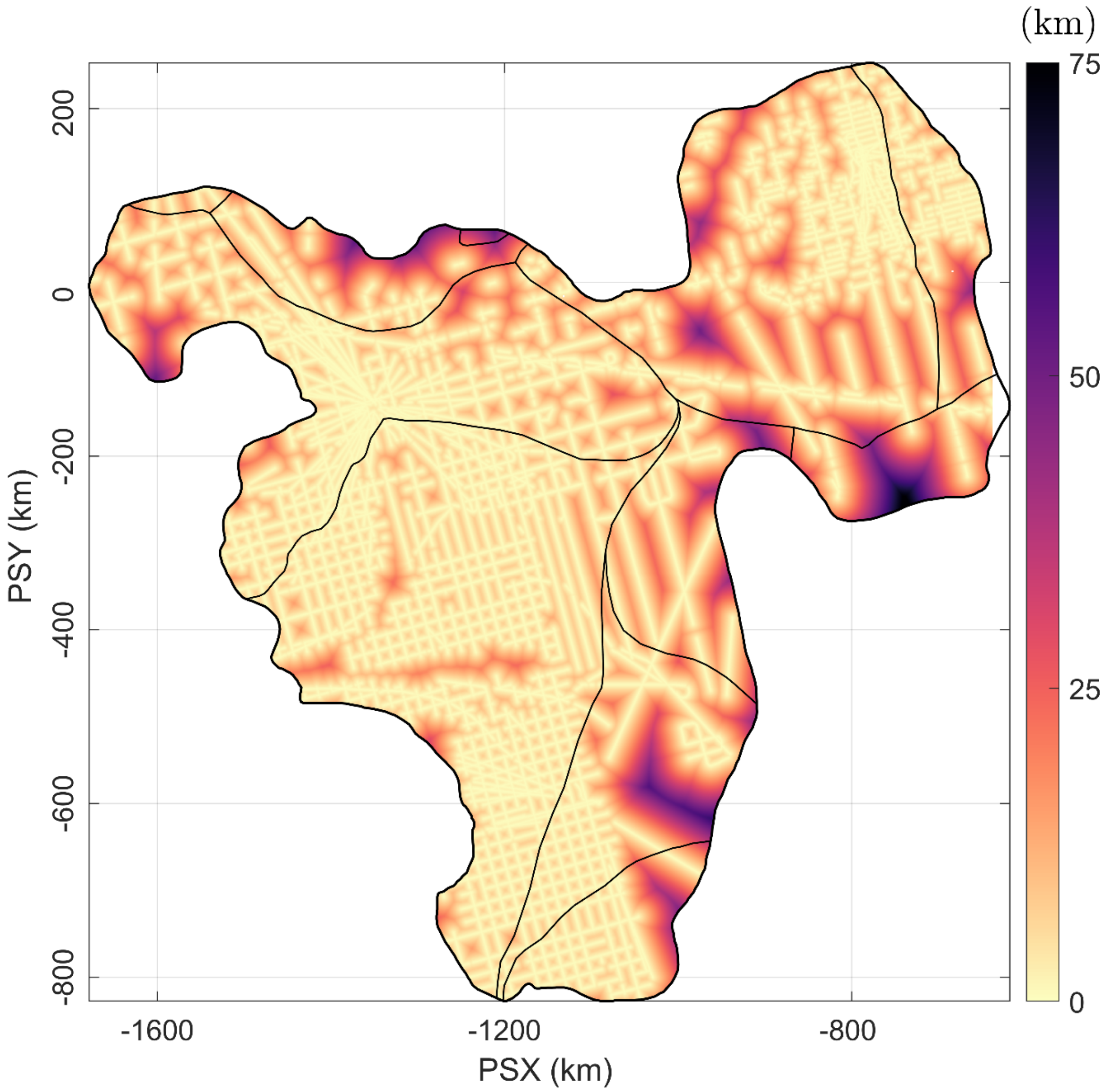

Figure S5. Maximum distance to the nearest 500-m along-track point used for the interpolation of the 4.72 ka IRH depth and accumulation grids.

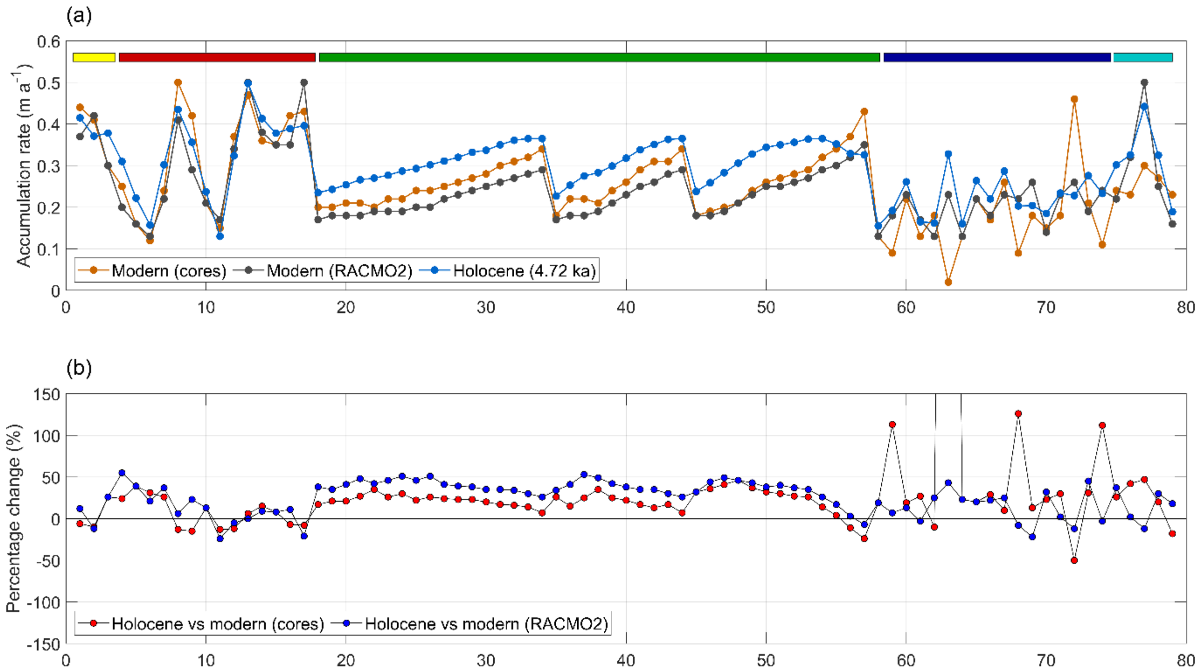

Figure S6. Scatter plot showing the difference in accumulation rates between the modern (cores and RACMO2) and the Holocene (4.72 ka) based on data showed in Figures 3c and 4 of the main paper. (a) Accumulation rates for each of Modern (cores), Modern (RACMO2), and Holocene (4.72 ka) at each of the 79 core locations shown in Figure 1. The five colour boxes at the top of (a) indicate the datasets to which each point belongs and are colour-coded as per the legend in Figure 1 (from left to right: MED14, ITASE, NEU08, SAMBA, SEAT-10). (b) Percentage change between Holocene and modern (cores; red) and Holocene and modern (RACMO2; blue) at the 79 core locations shown in Figure 1.